

## Research Article

# Research on Eddy Current Imaging Detection of Surface Defects of Metal Plates Based on Compressive Sensing

Weiquan Deng <sup>1,2</sup>, Bo Ye <sup>1,2</sup>, Guoyong Huang <sup>1,2</sup>, Jiande Wu <sup>1,2</sup>,  
Mengbao Fan <sup>3</sup>, and Jun Bao <sup>1,2</sup>

<sup>1</sup>Faculty of Information Engineering and Automation, Kunming University of Science and Technology, Kunming 650500, China

<sup>2</sup>Engineering Research Center for Mineral Pipeline Transportation of Yunnan Province, Kunming 650500, China

<sup>3</sup>School of Mechatronic Engineering, China University of Mining and Technology, Xuzhou 221116, China

Correspondence should be addressed to Guoyong Huang; hgymy@sina.com

Received 24 July 2018; Revised 5 October 2018; Accepted 30 October 2018; Published 8 November 2018

Academic Editor: Stefano Sfarra

Copyright © 2018 Weiquan Deng et al. This is an open access article distributed under the Creative Commons Attribution License, which permits unrestricted use, distribution, and reproduction in any medium, provided the original work is properly cited.

Accurate detection and quantitative evaluation of defects and damage in metal plates is a crucial task in a range of technological applications, such as maintaining the integrity, enhancing the safety, and assuring the reliability of structures. There is scope for improving eddy current testing methods by incorporating compressive sensing (CS) in the inspection process. The key scientific problems in eddy current imaging of defects of metal plates are sparse representations and transform domain mapping, sparse testing constraints, and sparse image reconstruction. The main research content of this paper is as follows. We first provide basic theory based on research of sparse representations, transform domain mapping, sparse matrices, sparse transform matrices, and signal recovery a priori errors. We then propose information-recovery methods for completing compressive sensing. Third, we establish an experimental system for validating theories and methods. Finally, we establish theories and methods for eddy current imaging of metal plates.

## 1. Introduction

Nondestructive testing refers to the use of electromagnetic, infrared, X-ray, ultrasonic, and other principles and techniques combined with instrumentation to detect defects and chemical and physical parameters of an object under the premise of not harming it or affecting its performance [1–5]. Among many nondestructive testing methods, eddy current nondestructive testing is widely used in metal material defect detection and performance evaluation due to its convenient operation, simple equipment, low cost, fast speed, and easy automatic online detection [6–8].

In recent years, many researchers have applied eddy current testing technology to solve the problems of metal material defect detection, identification, and classification [9–12]. Imaging technology overcomes the traditional nondestructive testing method, which can provide equivalent defect information but cannot obtain the defect shape. It has the advantages of intuitive defect information and good

visibility. At the same time, visualization is an important development that will shape eddy current testing instruments of the future. He et al. used a pulsed eddy current C-scan to detect the subsurface defects of aluminum alloy metal specimens and realized the identification, classification, and quantitative analysis of defects based on C-scan images [13]. Based on the principle of electromagnetic detection, Xu et al. used a C-scan to detect the welding surface of an X70 steel plate, and the C-scan imaging results were used to determine the hardness distribution of the welding surface of the test piece [14]. Ricci et al. used a multifrequency eddy current C-scan to image aluminum alloy defects and studied the effect of lift-off on defect imaging detection during the detection process [15]. Li et al. used an improved eddy current probe to detect the subsurface corrosion defects of metal materials by scanning imaging and determined that the depth information of the corrosion defects had a greater impact on defect imaging contrast [16]. However, in the current eddy current scanning imaging inspection of metal material

defects, full sampling of defects is a very time-consuming process. For example, with state-of-the-art technology, it takes about 6 min to scan a  $30 \times 30 \text{ mm}^2$  area at 0.25 mm resolution [14]. At the same time, the environment, equipment, and operation factors will affect the final defect imaging effect and the analysis and evaluation of defects during the testing process. By analyzing the characteristics of the defect eddy current signal, the signal-processing method is used to obtain the defect signal acquisition, reconstruction, imaging, and quantitative analysis, and the defect signal is processed to suppress noise interference during the detection process, enhancing the detection, imaging, and quantitative evaluation of metal material defects. In nondestructive detection imaging recognition, such as the defect and nondefect areas in defect detection, detection imaging contrast is enhanced by the signal-processing method, thereby improving the imaging recognition accuracy. Ahi analyzed the influence of the parameters in a THz imaging system using a mathematical model, and the THz images obtained by simulation had higher precision than those obtained by experiments [17]. On this basis, Ahi eliminated the interference of the signal in time and frequency domains and the low frequency spectrum by introducing a filter, enhancing the resolution of the imaging system [18]. This method is applied to the quality control and authentication of packaged integrated circuits [19], which greatly enhances the accuracy of a THz detection image. In recent years, increasing attention has been paid to the application of signal sparsity in nondestructive testing, especially in infrared thermal imaging nondestructive testing. Yousefi et al. adopted sparsity restriction to extract feature information of mineral ultrawide spectrum images by a sparse principal component analysis algorithm to realize automatic mineral recognition, achieving a higher classification accuracy [20, 21]. Wu et al. realized the thermal imaging detection of composite subsurface defects by a sparse principal component algorithm and enhanced the identification of material defect areas [22]. However, no research has reported on eddy current imaging based on signal sparsity analysis.

For this paper, within the theoretical framework of compressive sensing, we studied the basic theory, data-acquisition and signal-processing methods, and experimental testing of conductive structures using sparse eddy current imaging, enhancing the detection performance of imaging, realizing successful application, and providing theoretical and practical outcomes for nondestructive testing and evaluation of metal plates. We explored new approaches, improved the practice of nondestructive testing and evaluation technology, enhanced the testing level, strengthened its safety in operation, and eliminated hidden dangers of accidents. According to the analysis of the experimental results, the important contributions are summarized as follows.

(1) Based on the sparsity analysis of eddy current signals of metal sheet defects, this paper realizes the eddy current fast imaging detection and analysis of metal sheet defects by compression sensing, which is superior to traditional C-scan imaging in imaging speed and image quality.

(2) We have studied the relationship between the number of measurements and the sparsity of the signal. The experimental results show that the original signal can be reconstructed accurately when the number of measurements is four times the sparsity.

(3) We have studied the antinoise performance of the proposed method, and the experimental results show that the proposed method has strong antinoise performance.

The remainder of this paper is structured as follows. Section 2 describes the theoretical analysis of the methods used in this paper, including eddy current signal sparse characterization, observation matrix construction, and sparse signal reconstruction. Section 3 describes the experimental setup and specimen parameters used in this paper. The imaging effect and antinoise performance of different observation signals of sparse eddy current imaging methods are set and analyzed. The results of imaging, antinoise, and detection efficiency of the sparse eddy current imaging method are verified by traditional eddy current imaging methods. Finally, Section 4 contains our conclusions and discusses future research.

## 2. Theory of Sparse Imaging

Compressive sensing (CS) is a theory of signal acquisition, characterization, and process proposed by Donoho et al. in 2004 [23]. According to this theory, when there is no information loss, we can sample signals with a speed far lower than Nyquist sampling theory demands, transform the sampling signal to sampling information, and precisely restore the original signal. Therefore, compressive sensing is also called compressive sampling or sparse sampling [24, 25].

According to the principle of compressive sensing, suppose we have a vector  $x$  ( $N \times 1$ ) elements. We need to summarize  $x$  with some  $y$  that contains  $M \ll N$  elements. Simply put  $y = \Phi x$ ,  $\Phi$  here is the observation matrix. Thus  $\Phi$  is  $M \times N$  matrix. If  $x$  is a sparse matrix, we are endangered of losing most of nonzero elements of  $x$  while migrating to  $y$ . Fortunately, researchers have shown that if we use Gaussian random variables as our observation matrix  $\Phi$ , we will preserve our data with high probability. Now the big advantage of compressive sensing emerges. The vector  $x$  can be imagined as  $N$  sampling of a single while entitles  $M$  sampling of it. We can sample a signal in much less rate and it is a big advantage if sampling is time-consuming or cost driven.

The theory of compressive sensing mainly consists of three parts. Firstly, we have the sparse representation of the signal. Secondly, a matrix is designed to minimize the loss of the original signal while reducing the dimension. Finally, a signal reconstruction algorithm is designed to reconstruct the original signal without distortion by using a small number of observations. The three parts in the theoretical analysis will be discussed in detail in Sections 2.1, 2.2, and 2.3.

*2.1. Signal Sparseness Characteristic.* If signal  $x$  or its projection in the transform domain  $\Psi$  has few nonzero elements, then the signal is sparse and has a sparse property [23]. The

real signal  $x = (x_i)_{i=1}^N \in \mathbb{R}^N$  is called  $K$ -sparse if it satisfies the form

$$\|x\|_0 = \#\{i : x_i \neq 0\} \leq K, \quad (1)$$

where  $K$  is called the sparsity of the real signal  $x$ .

Most signals, or the transform coefficients in some transformation domains in nature, have sparsity, examples being the frequency domain transformation of time domain signals and the representation of image signals in the wavelet domain.

If the  $N$ -dimensional real signal  $x \in \mathbb{R}^{N \times 1}$  expands on an orthogonal basis  $\{\varphi_i\}_{i=1}^N$  ( $\varphi_i$  is an  $N$ -dimensional column vector), then

$$x = \sum_{i=1}^N \theta_i \varphi_i. \quad (2)$$

If the coefficient of the expansion  $\theta_i = \langle x, \varphi_i \rangle = \varphi_i^T x$ , then it can be described as

$$x = \Psi \theta, \quad (3)$$

where  $\Psi = [\varphi_1, \varphi_2, \dots, \varphi_n] \in \mathbb{R}^{N \times N}$  is the orthogonal basis (namely, dictionary matrix), and  $\theta = [\theta_1, \theta_2, \dots, \theta_N]^T$  is a coefficient vector [26]. If there are at most  $K$  nonzero elements in  $\theta$ , then  $\theta$  is  $K$ -sparse (usually the number of nonzero coefficients is much smaller than the original signal dimension, i.e.,  $K \ll N$ ).

**2.2. Observation Matrix Construction.** The compression sampling process can be expressed as a linear transformation as

$$y = \Phi x = \Phi \Psi \theta = \tilde{\Phi} \theta, \quad (4)$$

where  $\Phi : M \times N$  represents the observation matrix and  $\tilde{\Phi} = \Phi \Psi$  is called the sensing matrix, and so observation set  $y \in \mathbb{R}^{M \times 1}$  ( $M \ll N$ ).

Considering that the signal inevitably contains interference with noise  $e$  in practical applications, we can express (4) as

$$y = \tilde{\Phi} \theta + e. \quad (5)$$

To ensure that the observation set  $y$  contains enough information to reconstruct the original signal  $x$ , the observation matrix  $\Phi$  needs to satisfy the restricted isometry property (RIP); i.e.,

$$(1 - \delta_K) \|x\|_2^2 \leq \|\Phi x\|_2^2 \leq (1 + \delta_K) \|x\|_2^2, \quad (6)$$

where  $\delta_K \in (0, 1)$  is the constraint isometric constant of matrix  $\Phi$ . However, it is very difficult to construct an observation matrix that strictly satisfies the RIP property in practical application. Fortunately, Candès et al. proved the RIP property constraint of the observation matrix can be transformed to a correlation constraint between the observation and dictionary matrices [27]. When the observation

matrix is uncorrelated or weakly related to the dictionary matrix, the observation set  $y$  can contain enough information to reconstruct the original signal  $x$ . The correlation of the matrix is calculated as

$$\mu(\Phi, \Psi) = \max_{1 \leq i \leq M, 1 \leq j \leq N} |\langle \phi_i, \varphi_j \rangle|, \quad (7)$$

where  $\phi_i$  and  $\varphi_j$  are the row and column vectors of the observation matrix  $\Phi$  and dictionary matrix  $\Psi$ , respectively, and we know  $\mu(\Phi, \Psi) \in [1/\sqrt{n}, 1]$ . At the same time, the correlation between the observation and dictionary matrices will directly affect the observation number  $M$  of the final observation  $y$ . When the correlation  $\mu(\Phi, \Psi) = 1/\sqrt{n}$ , the minimum number of observations is required. When the correlation  $\mu(\Phi, \Psi) = 1$ , the observation matrix  $\Phi$  is equivalent to the identity matrix. At this time, the compressive sensing method degenerates into a conventional sampling method, and the number of samples will be equivalent to the original signal.

Candès and Romberg have proved that random Gaussian matrix with independent and identical distribution is uncorrelated to arbitrary orthogonal basis, and it can satisfy RIP with a large probability [28]. Therefore, we have used a random Gaussian matrix as the observation matrix in this paper.

**2.3. Sparse Signal Reconstruction.** Regarding defect imaging, we can acquire the observation set  $y = [y_1, y_2, \dots, y_M]^T$  by scanning  $M$  times. If there are  $N$  scanning points in the whole area, then we actually scan  $M$  times based on sparse sampling theory. If  $M < N$ ,  $M \geq O(K(\mu^2(\Phi, \psi) \log N))$  and  $K$  is the sparsity of the coefficient vector, then  $\mu(\Phi, \psi)$  is the correlation between the orthogonal basis dictionary matrix  $\psi$  and observation matrix  $\Phi$ .

To reconstruct the original signal from the observation set  $y$ , we consider the following method [29]:

$$\begin{aligned} \hat{x} &= \arg \min \|x\|_0 \\ \text{s.t. } & y = \Phi x. \end{aligned} \quad (8)$$

From the observation process of compressive sensing, the rows of the observation matrix  $\Phi$  are much smaller than the columns. Therefore, the solution of the underdetermined equation (8) is an NP-hard problem. For the 320 sample points where the defect is fully sampled in this paper, assume that the observation matrix  $\Phi$  has size  $60 \times 320$  when compressive sensing is performed ( $M=60, N=320$  and observed signal  $y \in \mathbb{R}^{60 \times 1}$ ). When reconstructing from (8), we must traverse all  $C_{320}^{60} \approx 6.6 \times 10^{65}$  options. If each traversal requires 1 ns, it will take  $2.1 \times 10^{48}$  years to traverse all the options. Fortunately, it was proved by Donoho and Candès that when the observation matrix  $\Phi$  satisfies the RIP condition in (6), the  $l_0$  minimization of (8) can be replaced by  $l_1$  minimization; i.e.,

$$\begin{aligned} \hat{x} &= \arg \min \|x\|_1 \\ \text{s.t. } & y = \Phi x. \end{aligned} \quad (9)$$

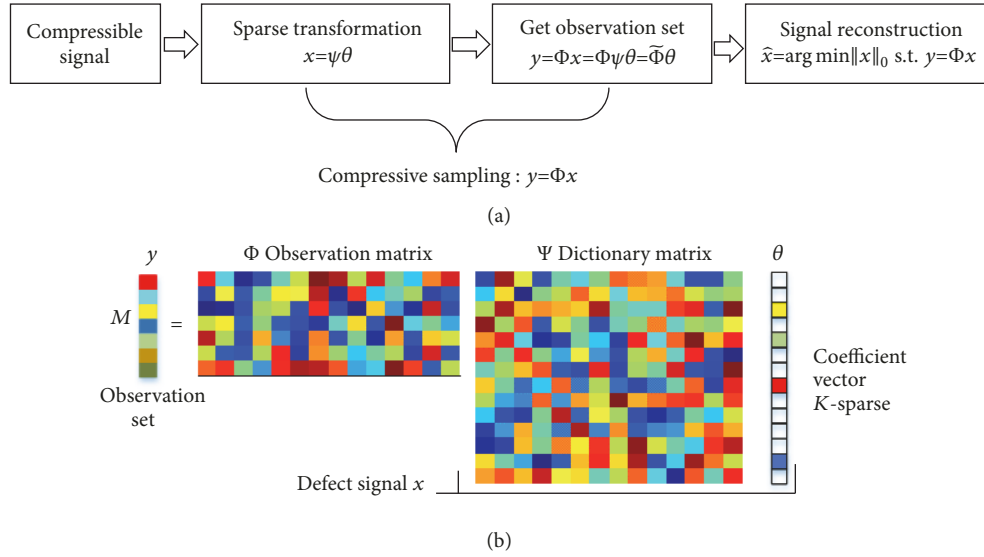


FIGURE 1: Sketch map of compressive sensing (a) and Sketch map of compressive sampling in the form of matrix-vector (b).

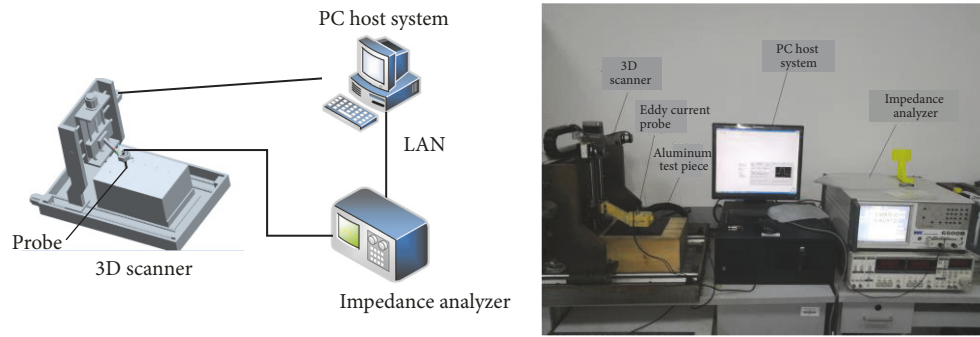


FIGURE 2: Automated experimental setup.

The above equation is signal reconstruction without noise interference. As in (5), when there is noise  $e$  during the observation and  $\|e\|_2 \leq \epsilon$ , the solution of (9) is converted as follows [30]:

$$\begin{aligned} \hat{x} = \arg \min \quad & \|x\|_1 \\ \text{s.t.} \quad & \|\Phi x - y\|_2 \leq \epsilon. \end{aligned} \quad (10)$$

In fact, Cai et al. have pointed out that when the constraint isometric constant  $\delta_K < 0.307$ , the observation matrix satisfies the condition for accurately reconstructing the signal  $x$  [31].

In summary, the compressive sensing process is shown in Figure 1(a), and the matrix representation of compression sampling vector is shown in Figure 1(b). As shown in Figure 1(b), the colored square in the coefficient vector represents a nonzero coefficient, and white represents a zero coefficient.

### 3. Experiment and Discussion

Figure 2 shows the automated experimental setup, which consists of a differential eddy current probe, impedance

analyzer, 3D mobile platform, and PC host system. The WK65120B impedance analyzer, produced by Wayne Kerr, is used to measure the impedance signal of the coil. Its measuring range is from 20 Hz to 120 MHz, with 0.05% measuring accuracy. The impedance analyzer communicates with the PC host system through a local area network. The PC host system records and processes impedance signals of the eddy current probe that come from the impedance analyzer. The LabView program in the PC host system operates motors along each axis through an MPC08 controller and drive, to move the eddy current probe along the programmed orbit. The 3D mobile platform is used to place and fix the testing piece and eddy current probe. The eddy current probe is a cylindrical air core coil with inside radius 2 mm, outside radius 2.4 mm, and height 5 mm. The coil is made of twining enamel insulated wire with 0.08 mm radius and 300 turns.

To verify the detection of crack defects and the effect of sparse imaging, nine crack defects of different length and depth were processed on the surface of a 3 mm thick 6061 aluminum plate by a wire cutting machine. The width of the defect was 1 mm, the length took the values 2 mm, 6

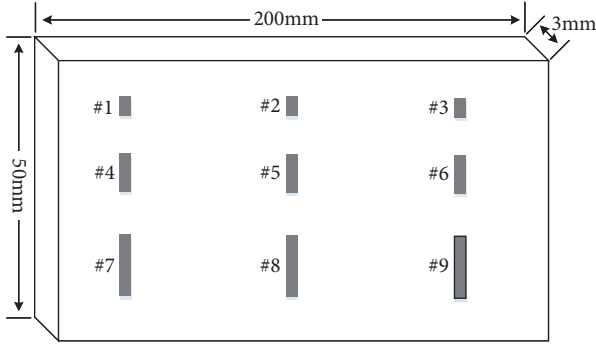


FIGURE 3: Size of aluminum testing piece and its defect distribution.

TABLE 1: Defect parameters of testing piece.

Defect number	Defect size (mm)		
	depth	length	width
#1	0.5	2	1
#2	1.5	2	1
#3	2.5	2	1
#4	0.5	6	1
#5	1.5	6	1
#6	2.5	6	1
#7	0.5	10	1
#8	1.5	10	1
#9	2.5	10	1

mm, and 10 mm, and the depth took values of 0.5 mm, 1.5 mm, and 2.5 mm. The defects in the horizontal and vertical directions of the test piece were the depth and length changes, respectively. The test piece size and defect distribution are shown in Figure 3. The crack defect parameters on the side of the test piece are shown in Table 1.

The scanning area of cracks and defects in this experiment was a  $16 \times 20 \text{ mm}^2$  rectangle containing a defect. The transverse and longitudinal intervals of the scanning points were both 1 mm. We gathered data from 320 ( $16 \times 20$ ) points in the entire scanning area. We scanned each point three times and took the average value as the impedance value of a point. We made an impedance image with the impedance values of the whole crack and defect area, with the imaging data displayed in Figure 4. An impedance image number corresponds to each defect number in the testing piece. From the impedance image in Figure 4, the impedance value of the crack area is obviously larger than that of the noncrack area, and we can clearly identify the size and direction of each defect. The contrast of the impedance image is increasingly obvious as the depth of the crack defect increases. The contrast change of the defect area in the impedance image coincides with the size and depth change of the aluminum alloy plate, and we can easily find the crack defect from the impedance image.

Figure 4 displays the complete sampling imaging outcome of impedance information of eddy current testing of

the aluminum plate testing piece with various defects. We scanned 320 points in each scanning area in the experiment, which was a time-consuming process. The probe of the eddy current testing continuously moves during scanning detection, which makes the detection signal itself quite dependable. The impedance image represents the electromagnetic scattering characteristic of the compound processed transient response between an excitation signal and the tested object under specific testing conditions. Scarcity of the eddy current imaging of the conductive material defects can be directly reflected in the transform domain of the eddy current imaging. Therefore, the original imaging data of metal plates defects and partial imaging data may have sparseness representation in their transform domain. This possibility should reveal a regular pattern of sparseness representation, thereby reducing scanning points of the testing piece in scanning and data collection to shorten detection time and accelerate the imaging process demand in defect identification. In the sparse sampling process, the sparsity of defect signal can be calculated by (1), which is the sparsity of #1, #2, and #3 is 18, the sparsity of #4, #5, and #6 is 35, and the sparsity of #7, #8, and #9 is 56. We used a Gaussian random matrix as observation matrix  $\Phi$  in the experiment, and the sensing matrix  $\bar{\Phi}$  could satisfy the restricted isometry property. Since the defect scanning impedance signal is a time-sparse signal, we used an identity matrix as the transform domain. When the testing number  $M \geq O(K(\mu^2(\Phi, \psi) \log N))$ , we can most likely recover the original signal after optimizing and reconstructing the original signal with the  $l_1$  norm [24, 25].

Under the condition  $M \geq O(K(\mu^2(\Phi, \psi) \log N))$ , we took sparse samples for defects #3, #6, and #9 in the test piece shown in Figure 3, and the signal was reconstructed for imaging. The reconstruction error and reconstruction time of the crack defect impedance image are shown in Figure 5. The reconstruction error is the root mean square error (RMSE) of the reconstructed signal and original signal,  $\text{RMSE} = \sqrt{(\sum_{i=1}^N (x_i - \hat{x}_i)^2)/N}$ .

*Note that.* the signal reconstruction algorithm in this article ran under the Windows 10 operating system and was configured as a 2.4-GHz Intel dual-core processor with 4 GB of RAM, running MATLAB version 2014a.

According to Figure 5, when the observation number  $M < 3.5 * K$  and  $K=18$ , reconstruction errors of differently sized defects all exceeded 0.005. The reconstruction errors continuously increased when the observed signal number decreased, and the time consumption of reconstruction constantly decreased. When the testing number  $M=3.5 * K$  and  $K=18$ , the reconstruction errors suddenly dropped to near zero, but the time consumption of reconstruction increased. Figures 6–8, respectively, show impedance images of the crack defect when  $M=4 * K$ , and  $K$  took values of 18, 35, and 56, respectively. Figure 9 shows the corresponding reconstruction errors of each impedance image of the crack defect.

Figures 6–9 show that the smaller the  $K$  value, the greater the sparsity, and the poorer the impedance image

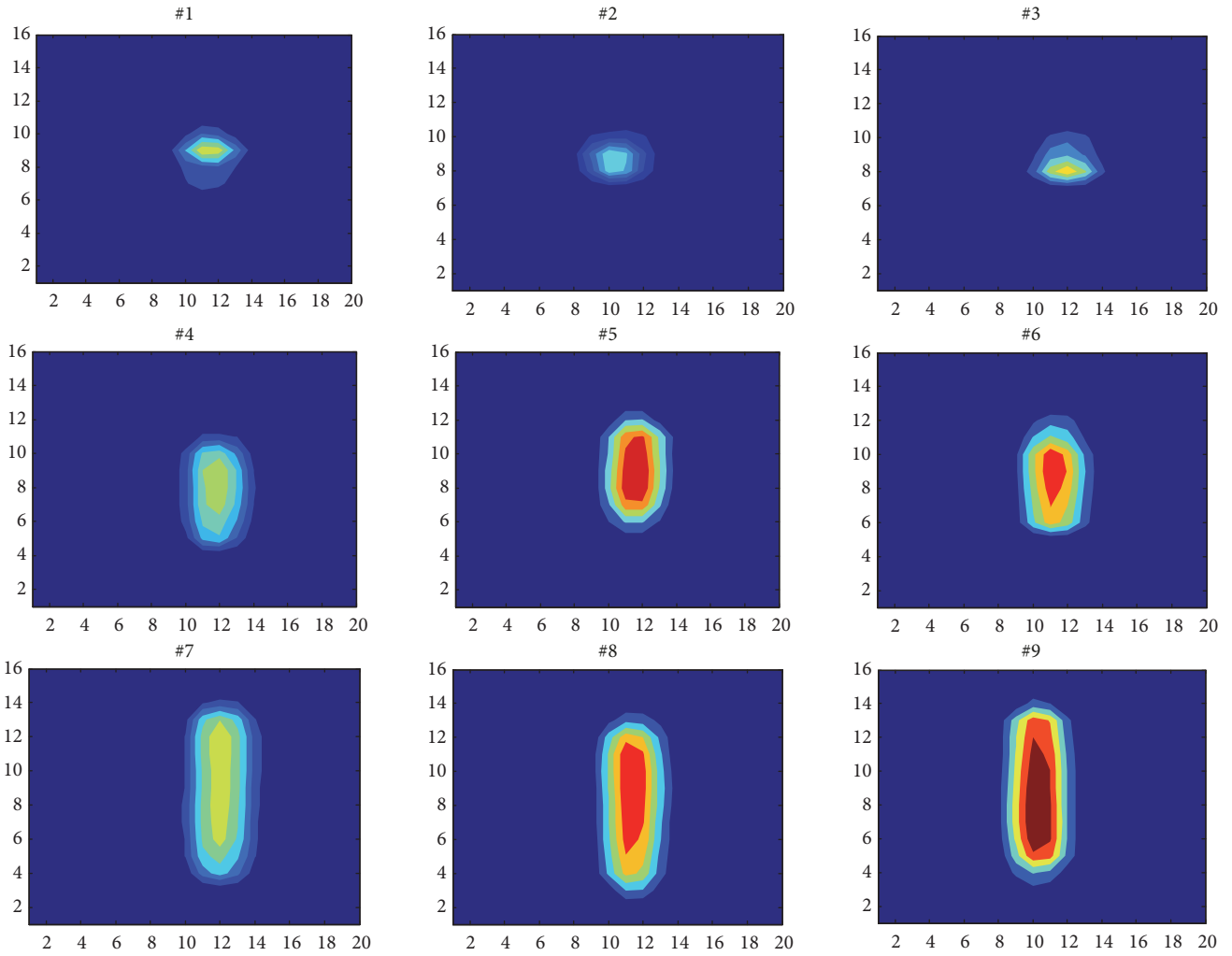


FIGURE 4: Original scanning imaging of aluminum testing piece.

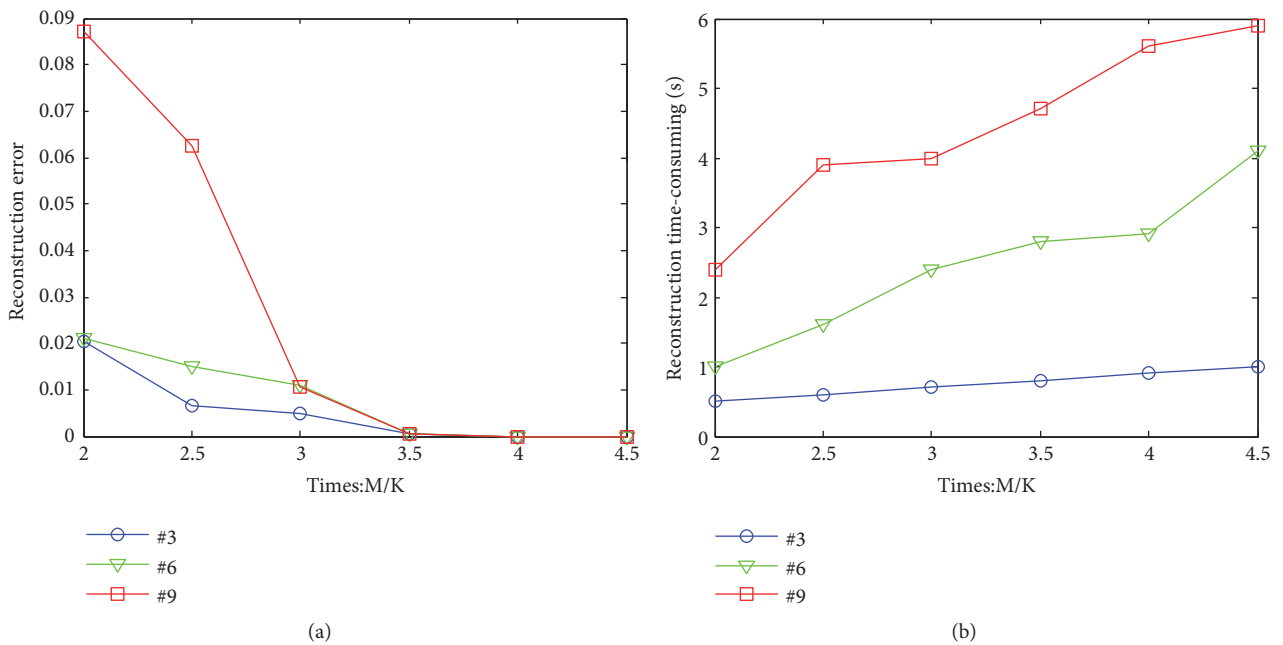


FIGURE 5: Reconstruction errors (a) and time consumption of reconstruction (b).

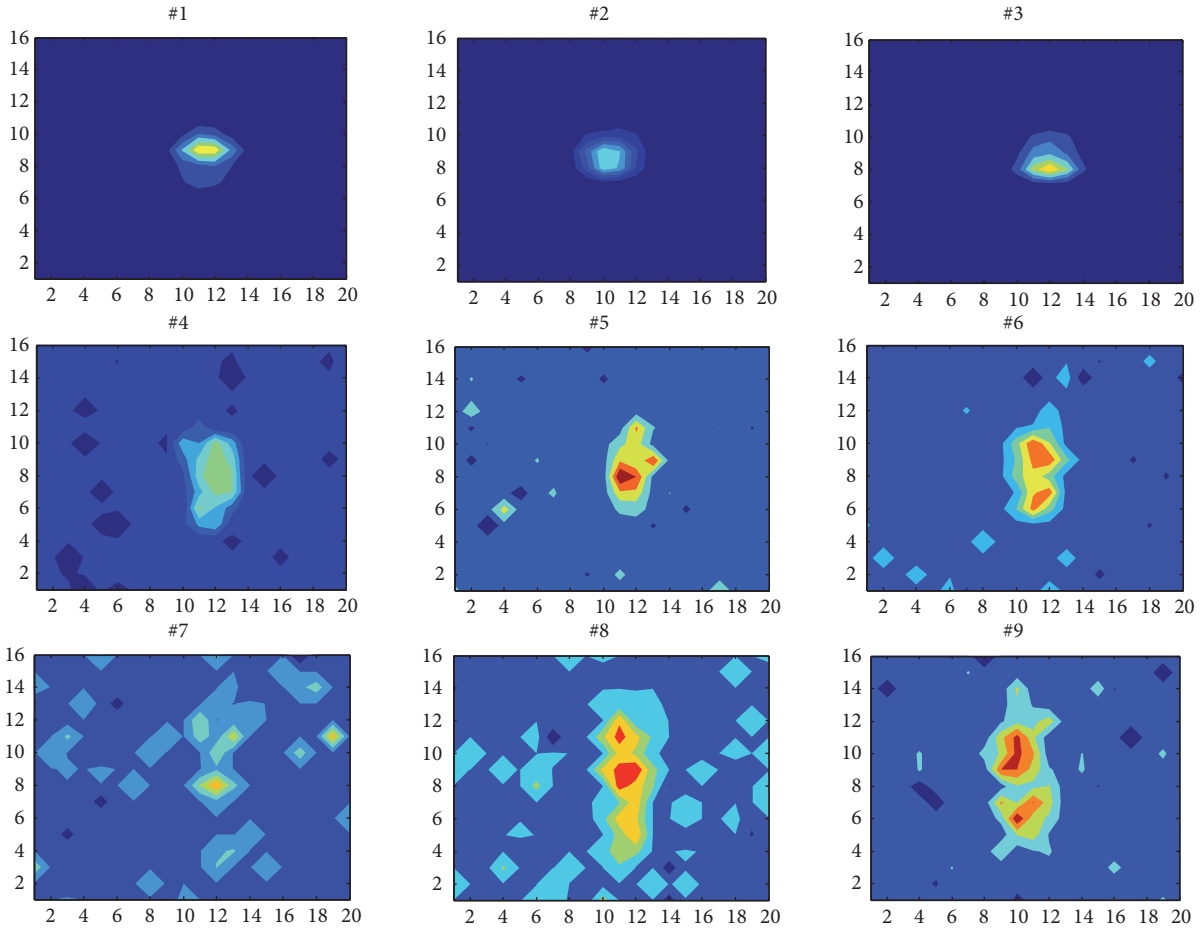


FIGURE 6: Impedance image of crack defect ( $M=4*K$ ,  $K=18$ ).

reconstruction effect of the same crack defect, the larger the reconstruction errors. When we set a smaller  $K$  value and a larger sparsity, the obtained signal information suffers great loss, and the reconstruction errors of the impedance image of the crack defect will grow as the area of the crack defect increases.

Figure 10 shows the reconstruction errors of the impedance image of defect #2 with different signal-to-noise ratios when we introduce Gaussian white noise. From Figure 10, we find that the smaller the  $M$  value, the greater the sparsity and reconstruction errors. At the same time, the reconstruction errors will grow when the noise increases and the signal-to-noise ratios decrease.

Figures 11(a)–11(f) show impedance images of the crack defect when  $M=4*K$  with signal-to-noise ratios 60 dB, 50 dB, 40 dB, 30 dB, 20 dB, and 10 dB, respectively, and corresponding reconstruction errors of 0.0000659, 0.000434, 0.0011, 0.028, 0.008, and 0.02. From Figure 11, we find that when the noise level increases, the reconstruction errors of the whole image increase and the imaging effects deteriorate, but the impedance image effect of the crack defect site keeps well and will not influence follow-up quantifying evaluations of the site and size of the crack defect.

## 4. Conclusion

We conducted a detailed study on the basic theory, data-acquisition methods, and signal-processing methods in the theory of compressive sensing, followed by experimental testing. Under the premise of ensuring no information loss, defect detection was carried out at far fewer sampling points than a full sampling scan on a test piece, and we studied eddy current imaging and imaging reconstruction with different sparsity and generated the corresponding reconstruction errors. We also conducted imaging reconstruction with the eddy current detection signal combined with noise and generated the corresponding reconstruction errors. We reached the following conclusions.

First, in accordance with the sparse feature of the eddy current detection signal of crack defects, we can set a corresponding observation matrix, sample the eddy current detection signal with a frequency far below that of the Nyquist sampling theorem, and generate the impedance reconstruction image of a crack defect with the corresponding reconstruction algorithm. The greater the sparsity, the greater the reconstruction errors of the crack

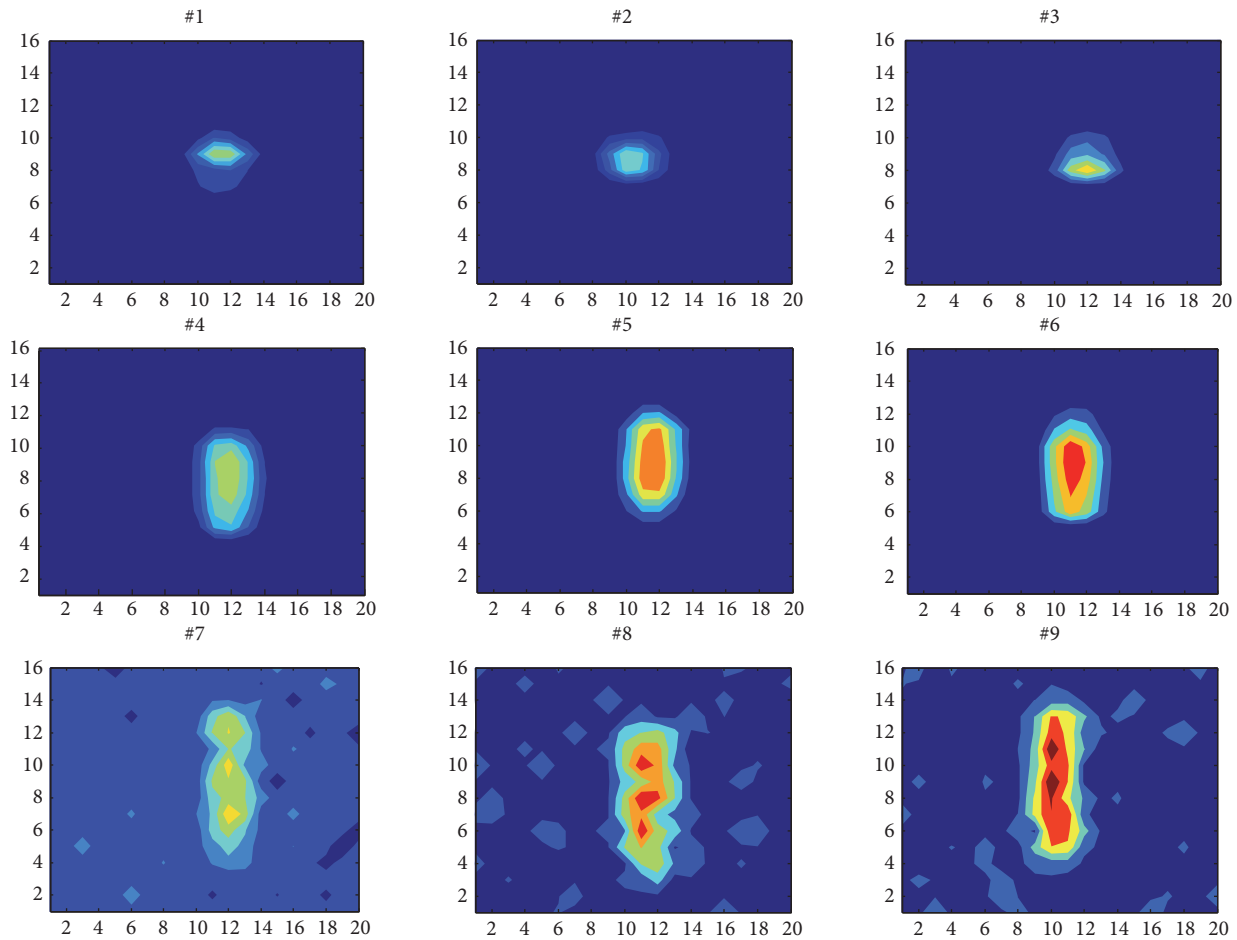


FIGURE 7: Impedance image of crack defect ( $M=4*K$ ,  $K=35$ ).

defect image, but the reconstruction time decreases to some extent, and the reconstruction speed increases considerably.

Second, the smaller the  $K$  value, the greater the sparsity, and the poorer the impedance image reconstruction effect of the same crack defect, the larger the reconstruction errors. When we set a smaller  $K$  value and a larger sparsity, signal information is lost, and the reconstruction errors of the impedance image of the crack defect will grow as the area of the crack defect increases.

Third, when the noise level increases, the reconstruction errors of the whole image increases and the imaging effects deteriorate. However, the impedance image effect of the crack defect site keeps well and will not influence a follow-up quantifying evaluation of the site and size of the crack defect.

The imaging detection of eddy current defects overcomes the fact that the traditional nondestructive testing method can only give equivalent defect information and cannot obtain the defect shape. It has intuitionistic and visual advantages, but in the traditional eddy current imaging method of full sampling detection of defects, the scanning of the defect is time-consuming. At the same time, the full sampling information includes much redundancy, which

causes waste in storage. In this paper, the detection method of the compressive sensing defect imaging based on the sparsity of defect signal was used to detect defect information through limited observation of the defect, which improved the efficiency of defect detection. It provides a new idea for the rapid detection and performance evaluation of metal plates defects and improves the state of eddy current detection technology.

Since the signal reconstruction method in this paper has a large reconstruction error under a low signal-to-noise ratio, our next work will focus on optimizing the reconstruction algorithm to improve its antinoise capability and improve the imaging effect of defect reconstruction under strong noise interference.

## Data Availability

The [54\_ECScanRows.mat] data used to support the findings of this study have been deposited in the [mcolab of Kunming University of Science and Technology] repository ([[http://mcolab.kmust.edu.cn/otherData/ECdata\\_%20OriginalData.rar](http://mcolab.kmust.edu.cn/otherData/ECdata_%20OriginalData.rar)]), and other researchers can download original data from this URL. The experimental equipment setup

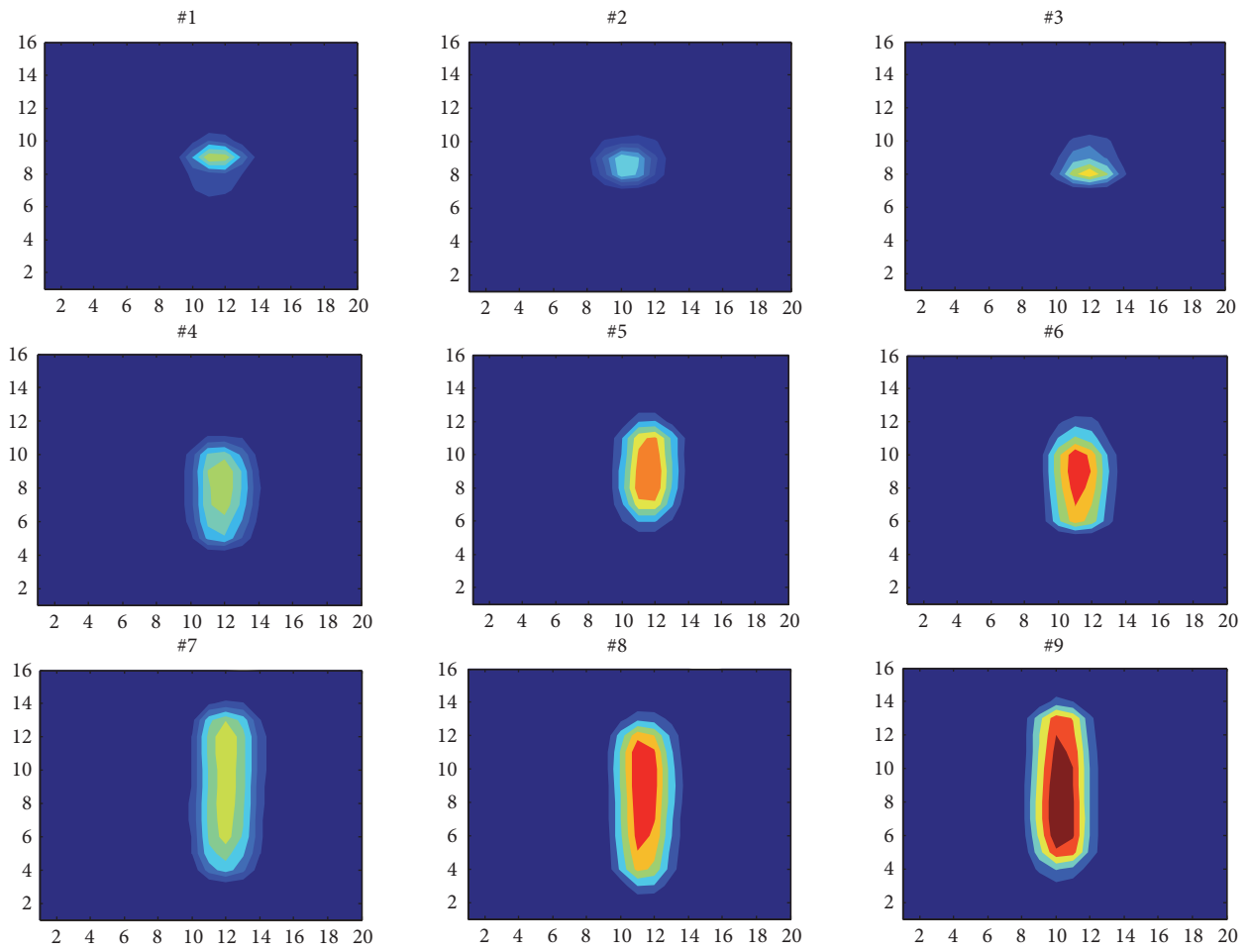


FIGURE 8: Impedance image of crack defect ( $M=4 * K, K=56$ ).

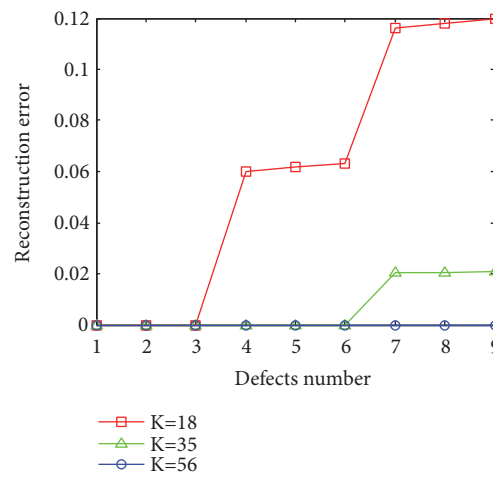


FIGURE 9: Reconstruction errors of each impedance image of the crack defect.

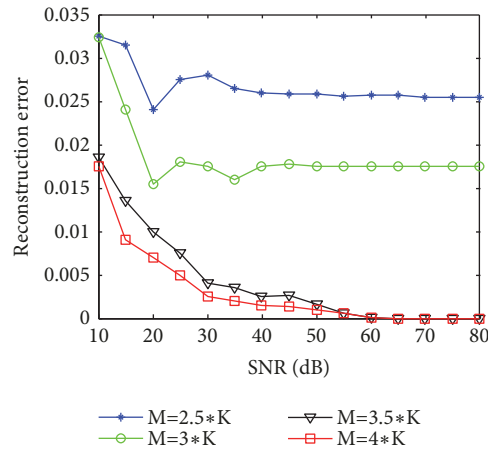


FIGURE 10: Reconstruction errors of impedance signal with different signal-to-noise ratios.

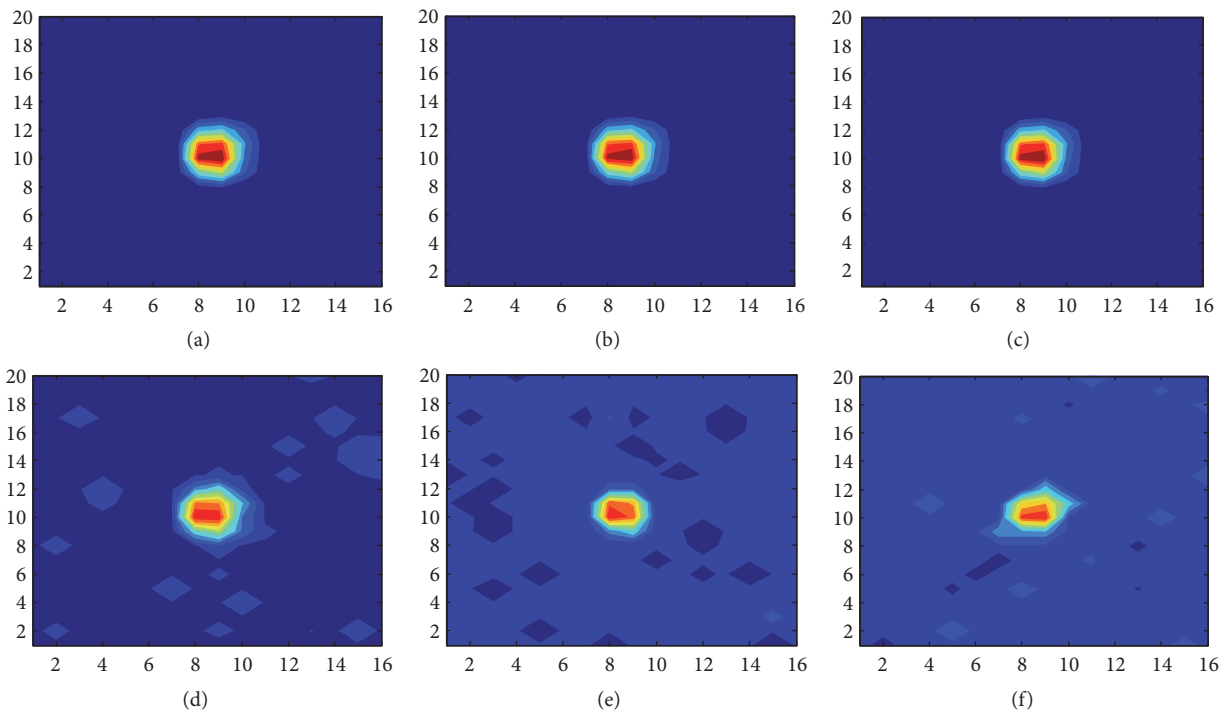


FIGURE 11: Impedance image of crack defect with different signal-to-noise ratios ( $M=4*K$ ,  $K=18$ ).

and testing piece parameters are shown in Figure 2 and Table 1.

### Conflicts of Interest

The authors declare that they have no conflicts of interest.

### Acknowledgments

This work is supported by the National Natural Science Foundation of China under the Grant nos. 51465024 and 51105183.

### References

- [1] M. V. Felice, A. Velichko, and P. D. Wilcox, "Accurate depth measurement of small surface-breaking cracks using an ultrasonic array post-processing technique," *NDT & E International*, vol. 68, pp. 105–112, 2014.
- [2] Y. Zou, D. Du, B. Chang, L. Ji, and J. Pan, "Automatic weld defect detection method based on Kalman filtering for real-time radiographic inspection of spiral pipe," *NDT & E International*, vol. 72, pp. 1–9, 2015.
- [3] G. Y. Tian, Y. He, L. Cheng, and P. Jackson, "Pulsed eddy current thermography for corrosion characterisation," *International Journal of Applied Electromagnetics and Mechanics*, vol. 39, no. 1–4, pp. 269–276, 2012.

- [4] S. Sfarra, P. Theodorakeas, C. Ibarra-Castanedo et al., "Evaluation of defects in panel paintings using infrared, optical and ultrasonic techniques," *Insight: Non-Destructive Testing and Condition Monitoring*, vol. 54, no. 1, pp. 21–27, 2012.
- [5] S. Sfarra, C. Ibarra-Castanedo, C. Santulli et al., "Falling weight impacted glass and basalt fibre woven composites inspected using non-destructive techniques," *Composites Part B: Engineering*, vol. 45, no. 1, pp. 601–608, 2013.
- [6] M. Fan, B. Cao, A. I. Sunny, W. Li, G. Tian, and B. Ye, "Pulsed eddy current thickness measurement using phase features immune to liftoff effect," *NDT & E International*, vol. 86, pp. 123–131, 2017.
- [7] D. Wen, M. Fan, B. Cao, B. Ye, and G. Tian, "Lift-Off Point of Intersection in Spectral Pulsed Eddy Current Signals for Thickness Measurement," *IEEE Sensors Letters*, vol. 2, no. 2, pp. 1–4, 2018.
- [8] X. Chen, D. Hou, L. Zhao, P. Huang, and G. Zhang, "Study on defect classification in multi-layer structures based on Fisher linear discriminate analysis by using pulsed eddy current technique," *NDT & E International*, vol. 67, pp. 46–54, 2014.
- [9] T. Chen, G. Y. Tian, A. Sophian, and P. W. Que, "Feature extraction and selection for defect classification of pulsed eddy current NDT," *NDT & E International*, vol. 41, no. 6, pp. 467–476, 2008.
- [10] Y. He, F. Luo, M. Pan et al., "Pulsed eddy current technique for defect detection in aircraft riveted structures," *NDT & e International*, vol. 43, pp. 176–181, 2010.
- [11] B. Liu, P. Huang, X. Zeng, and Z. Li, "Hidden defect recognition based on the improved ensemble empirical decomposition method and pulsed eddy current testing," *NDT & E International*, vol. 86, pp. 175–185, 2017.
- [12] K. B. Ali, A. N. Abdalla, D. Rifai, and M. A. Faraj, "Review on system development in eddy current testing and technique for defect classification and characterization," *IET Circuits, Devices & Systems*, vol. 11, no. 4, pp. 330–343, 2017.
- [13] Y. He, M. Pan, F. Luo, and G. Tian, "Pulsed eddy current imaging and frequency spectrum analysis for hidden defect nondestructive testing and evaluation," *NDT & E International*, vol. 44, no. 4, pp. 344–352, 2011.
- [14] H. Xu, J. R. S. Avila, F. Wu et al., "Imaging x70 weld cross-section using electromagnetic testing," *NDT & E International*, vol. 98, pp. 155–160, 2018.
- [15] M. Ricci, G. Silipigni, L. Ferrigno, M. Laracca, I. D. Adewale, and G. Y. Tian, "Evaluation of the lift-off robustness of eddy current imaging techniques," *NDT & E International*, vol. 85, pp. 43–52, 2017.
- [16] Y. Li, S. Ren, B. Yan, I. M. Z. Abidin, and Y. Wang, "Imaging of subsurface corrosion using gradient-field pulsed eddy current probes with uniform field excitation," *Sensors*, vol. 17, no. 8, 2017.
- [17] K. Ahi, "Mathematical modeling of thz point spread function and simulation of THz imaging systems," *IEEE Transactions on Terahertz Science and Technology*, vol. 7, no. 6, pp. 747–754, 2017.
- [18] K. Ahi, "A Method and System for Enhancing the Resolution of Terahertz Imaging," *Measurement*, 2018.
- [19] K. Ahi, S. Shahbazmohamadi, and N. Asadizanjani, "Quality control and authentication of packaged integrated circuits using enhanced-spatial-resolution terahertz time-domain spectroscopy and imaging," *Optics and Lasers in Engineering*, vol. 104, pp. 274–284, 2018.
- [20] B. Yousefi, S. Sojasi, and C. I. Castanedo, "Mineral identification in hyperspectral imaging using Sparse-PCA," in *Proceedings of the SPIE Commercial + Scientific Sensing and Imaging*, 2016.
- [21] B. Yousefi, S. Sojasi, C. I. Castanedo et al., "Comparison assessment of low rank sparse-PCA based-clustering/classification for automatic mineral identification in long wave infrared hyperspectral imagery," *Infrared Physics & Technology*, vol. 93, pp. 103–111, 2018.
- [22] J.-Y. Wu, S. Sfarra, and Y. Yao, "Sparse Principal Component Thermography for Subsurface Defect Detection in Composite Products," *IEEE Transactions on Industrial Informatics*, 2018.
- [23] D. L. Donoho, "Compressed sensing," *IEEE Transactions on Information Theory*, vol. 52, no. 4, pp. 1289–1306, 2006.
- [24] E. J. Candès and M. B. Wakin, "An introduction to compressive sampling," *IEEE signal processing magazine*, vol. 25, no. 2, pp. 21–30, 2008.
- [25] M. F. Duarte, M. A. Davenport, D. Takbar et al., "Single-pixel imaging via compressive sampling: Building simpler, smaller, and less-expensive digital cameras," *IEEE Signal Processing Magazine*, vol. 25, no. 2, pp. 83–91, 2008.
- [26] H. Rauhut, K. Schnass, and P. Vandergheynst, "Compressed sensing and redundant dictionaries," *IEEE Transactions on Information Theory*, vol. 54, no. 5, pp. 2210–2219, 2008.
- [27] E. Candès and J. Romberg, "Sparsity and incoherence in compressive sampling," *Inverse Problems*, vol. 23, no. 3, pp. 969–985, 2007.
- [28] E. J. Candès, J. Romberg, and T. Tao, "Robust uncertainty principles: exact signal reconstruction from highly incomplete frequency information," *Institute of Electrical and Electronics Engineers Transactions on Information Theory*, vol. 52, no. 2, pp. 489–509, 2006.
- [29] Y. Wiaux, L. Jacques, G. Puy, A. M. M. Scaife, and P. Vandergheynst, "Compressed sensing imaging techniques for radio interferometry," *Monthly Notices of the Royal Astronomical Society*, vol. 395, no. 3, pp. 1733–1742, 2009.
- [30] C. A. Metzler, A. Maleki, and R. . Baraniuk, "From denoising to compressed sensing," *Institute of Electrical and Electronics Engineers Transactions on Information Theory*, vol. 62, no. 9, pp. 5117–5144, 2016.
- [31] T. T. Cai, L. Wang, and G. Xu, "New bounds for restricted isometry constants," *IEEE Transactions on Information Theory*, vol. 56, no. 9, pp. 4388–4394, 2010.

